Analytical and Bioanalytical Chemistry (2019) 411:3497–3506
https://doi.org/10.1007/s00216-019-01827-w

RESEARCH PAPER

High-resolution laser ablation inductively coupled plasma mass spectrometry used to study transport of metallic nanoparticles through collagen-rich microstructures in fibroblast multicellular spheroids

Akihiro Arakawa[1,2] · Norbert Jakubowski[3] · Sabine Flemig[1] · Gunda Koellensperger[4] · Mate Rusz[4,5] · Daigo Iwahata[2] · Heike Traub[1] · Takafumi Hirata[6]

Received: 18 February 2019 / Revised: 22 March 2019 / Accepted: 2 April 2019 / Published online: 25 April 2019

Abstract

We have efficiently produced collagen-rich microstructures in fibroblast multicellular spheroids (MCSs) as a three-dimensional in vitro tissue analog to investigate silver (Ag) nanoparticle (NP) penetration. The MCS production was examined by changing the seeding cell number (500 to 40,000 cells) and the growth period (1 to 10 days). MCSs were incubated with Ag NP suspensions with a concentration of 5 μg mL^{-1} for 24 h. For this study, laser ablation inductively coupled plasma mass spectrometry (LA-ICP-MS) was used to visualize Ag NP localization quantitatively. Thin sections of MCSs were analyzed by LA-ICP-MS with a laser spot size of 8 μm to image distributions of ^{109}Ag, ^{31}P, ^{63}Cu, ^{66}Zn, and ^{79}Br. A calibration using a NP suspension was applied to convert the measured Ag intensity into the number of NPs present. The determined numbers of NPs ranged from 30 to 7200 particles in an outer rim of MCS. The particle distribution was clearly correlated with the presence of ^{31}P and ^{66}Zn and was localized in the outer rim of proliferating cells with a width that was equal to about twice the diameter of single cells. Moreover, abundant collagens were found in the outer rim of MCSs. For only the highest seeding cell number, NPs were completely captured at the outer rim, in a natural barrier reducing particle transport, whereas Eosin (^{79}Br) used as a probe of small molecules penetrated into the core of MCSs already after 1 min of exposure.

Keywords Laser ablation inductively coupled plasma mass spectrometry · Silver nanoparticles · Fibroblast cells · Multicellular spheroids

Electronic supplementary material The online version of this article (https://doi.org/10.1007/s00216-019-01827-w) contains supplementary material, which is available to authorized users.

✉ Akihiro Arakawa
akihiro.arakawa@bam.de; akihiro_arakawa@ajinomoto.com

[1] Bundesanstalt für Materialforschung und -prüfung (BAM), Richard Willstätter-Str. 11, 12489 Berlin, Germany

[2] Research Institute for Bioscience Products and Fine Chemicals, Ajinomoto Co., Inc., 1-1 Suzuki-cho, Kawasaki-shi, Kanagawa 210-8681, Japan

[3] Spetec GmbH, Berghamer Str. 2, 85435 Erding, Germany

[4] Institute of Analytical Chemistry, University of Vienna, Währinger-Str. 38, 1090 Vienna, Austria

[5] Cell Culture Facility, Institute of Inorganic Chemistry, University of Vienna, Althanstrasse 14 (UZA II), 1090 Vienna, Austria

[6] Geochemical Research Center, The University of Tokyo, Hongo, 7-3-1, Bunkyo-ku, Tokyo 113-0033, Japan

Introduction

Nanomaterials are currently applied in a variety of consumer products and are widely used in human daily life [1]. Silver (Ag) nanoparticles (NPs), which are one type of commonly used nanomaterials, are included in cosmetics and textiles because of their high antimicrobial activity [2]. Ag NPs are also attractive for numerous medical applications, for instance, in clinical diagnostics and wound dressings [3, 4]. With their widespread use, the potential for human exposure to Ag NPs—either intended or unintended—is increasing. Therefore, many studies have evaluated the toxicity and toxicity mechanisms of Ag NPs through in vivo and in vitro studies using animal models or cell cultures [5] and methods such as optical and dark-field microscopy [6], surface-enhanced Raman scattering [7–9], and photothermal microscopy [10, 11]. However, these characterization methods do

not provide quantitative data. Electron and X-ray microscopy [12] as well as slice and view techniques [13] using a focused ion beam and scanning electron microscopy are in principle capable of providing precise information about NP distributions but require complicated preparation procedures and are time consuming.

Inorganic metallic NPs can be quantified by inductively coupled plasma mass spectrometry (ICP-MS) after digestion of the cell suspension [14, 15] or by laser ablation (LA)-ICP-MS, which has been recently reviewed [16]. LA-ICP-MS is a convenient method for elemental bioimaging of tissue sections because it possesses the advantages of easy sample preparation, multi-element detection with high sensitivity, and high spatial resolution [17]. For tissue imaging, Vanhaeke and colleagues reported high-resolution LA-ICP-MS with (sub-)cellular spatial resolution [18]. This approach was applied by Giesen et al. [19] for single cell analysis for the first time and then later by Drescher et al. [20] to detect gold (Au) NPs and Ag NPs in single fibroblast cells. A calibration procedure using NP suspensions was described in the latter work. LA-ICP-MS has also been used for bioimaging to study transport of very small iron oxide NPs in a mouse model to confirm enrichment of these NPs in atherosclerotic plaques to develop a new contrast agent for magnetic resonance imaging [21].

Recently, LA-ICP-MS has been used in combination with SERS to correlate the signals of Au NPs with LA-ICP-MS [22] and compare the uptake of metallic and silica-coated metallic NPs [23]. In comparison to single cell experiments, multicellular spheroids (MCSs) have been developed to serve as a three-dimensional (3D) in vitro model to reproduce a microenvironment typical of tissues or tumors and to study the diffusion or active transport of drugs. Theiner et al. [24, 25] were the first to use LA-ICP-MS to image platinum (Pt)–based cancer therapy drugs in thin sections of tumor MCSs. A heterogenous distribution of Pt was observed in thin sections of different MCSs with the highest Pt concentrations in the center and the outer cell layer of the tumor MCSs. In 2001, Furukawa and coworkers cultured normal human skin fibroblast MCSs with a biodegradable scaffold with the goal of producing tissue-engineered skin and skin repair materials [26]. They overcame the challenge of adhesion of cells by coating the glassware and a rotational culture. Priwitaningrum et al. [27] developed and characterized a 3D co-culture of fibroblast and tumor cell MCSs with a seeding cell number of 2×10^6 to mimic a tumor stroma and investigated the penetration of fluorescently labeled NPs into these MCSs. They qualitatively found that stroma-like MCSs acted as a barrier for NP penetration depending on incubation time and stroma composition, which is an important finding for applications in nanomedicine. However, quantitative data were not presented. Jorgenson et al. [28] studied transcriptional effectors for initiating fibroblast activation and tissue fibrosis. They cultured fibroblast cells in hanging drops with only 500 cells per droplet.

For investigations to study the microenvironment of tissues, fibroblast cells are necessary because they secrete abundant extracellular matrix including growth factors and collagens [29, 30]. However, as shown in previous studies, seeding cell numbers differ significantly and thus comparison of results are complicated in particular if the interaction with nanoparticles should be investigated.

Therefore, it is the aim of this study to examine how the seeding cell number of fibroblast cells affects the built-up of a natural barrier. Ag NPs and Eosin were used as probes for particles and small molecules. In this study, Eosin is used as an exogenous molecule containing Br atoms, which can be detected by ICP-MS, to examine the diffusion of small molecules such as nutrients. For this purpose, a LA-ICP-MS was used to visualize localization of both probes. For Ag NPs, the particle number was quantified by a calibration based on NP suspensions using a well-established matrix-matched approach [20].

Experimental section

Reagents

Dulbecco's modified Eagles medium (DMEM), fetal bovine serum (FBS), eosin ($C_{20}H_8Br_2N_2O_9$, molecular weight 647), 4′,6-diamidine-2′-phenylindole dihydrochloride (DAPI), aniline blue solution, trypan blue, and ultra-pure water were purchased from Merck KGaA (Darmstadt, Germany). Tris-buffered saline (TBS) was purchased from Th. Geyer GmbH & Co. KG (Renningen, Germany). Acetic acid was purchased from AppliChem GmbH (Darmstadt, Germany). Citrate-coated Ag NPs with a diameter of 50 nm were purchased from nanoComposix Inc. (CA, USA).

Production of MCSs

To produce MCSs, a different cell line was selected for comparison with our previous work [25]. NIH-3T3 cells (Swiss albino mouse fibroblast cells, DSMZ, Braunschweig, Germany), an adherent cell line, were harvested from culture flasks by trypsinization and then cells were counted with a hemocytometer (C-Chip, Labteck International Ltd., Heathfield, UK) after staining with trypan blue. The diameter of cells was measured by a Scepter™ cell counter (Merck KGaA) using an aliquot of the cell suspension. The cell suspension was diluted in several concentrations with DMEM containing 10% FBS and then 300 μL of each sample was put into individual wells of a non-cell culture-treated round bottom 96-well plate (Nunclon™ Sphera™, VWR International GmbH, Darmstadt, Germany). The well plate was coated by a hydrogel to avoid adhesion of the fibroblast cells. Only one spheroid was grown per well. The growing

period was investigated from 1 to 10 days, after which the diameter of the spheroid became constant. For this purpose, cell cultures were maintained at 37 °C in a humidified atmosphere containing 95% air and 5% carbon dioxide. Half of the volume of medium in each well was changed every 4 days. The diameter of MCSs was measured by an optical microscope (AE2000, Motic (Xiamen) Electric Group Co., Ltd., Xiamen, China).

Sample preparation of spheroids for LA-ICP-MS

NPs were suspended in DMEM containing 10% FBS to give a concentration of 10 μg mL^{-1} based on the mass of Ag. An aliquot of the suspension (150 μL) was put into each well after the same volume of medium was removed. After the incubation, each MCS was washed with TBS, stained with 0.5% (*w*/*v*) eosin for 1 min, washed with TBS again, transferred into a 1.5-mL Eppendorf tube, and then washed twice with TBS (500 μL). Each MCS was transferred into a plastic container (Cryomold®, Sakura Finetek USA, Inc., CA, USA) in which it was embedded using Tissue-Tek® (Sakura Finetek USA, Inc.) and then stored at − 80 °C. The embedded quadratic blocks with a length 10 mm and thickness of 5 mm were sectioned into slices with a thickness of 20 μm by a cryomicrotome (CM3050S, Leica Biosystems Nussloch GmbH, Nussloch, Germany). The thin sections were placed on microscope slides (SuperFrost Plus™, Thermo Fisher Scientific Inc., MA, USA) for imaging.

Calibration using NP spots on nitrocellulose membrane

The NP content of cells was quantified in accordance with Drescher et al. [20] by spotting standards onto nitrocellulose film slides (ONCYTE® SuperNova, Merck KGaA). For this purpose, a calibration series of NP suspensions with given particle number concentrations were printed on the slides using a non-contact piezo-driven array spotter (Scienion US Inc., Berlin, Germany). Arraying was repeated ten times using a volume of 350 pL and a diameter of around 130 μm. For calibration, the printed spots on the slide were ablated in a single-spot ablation mode by selecting a laser diameter of 175 μm, which was slightly larger than the array spot diameter. The LA-ICP-MS settings are summarized in Table 1. The calibration spot was ablated completely. For each calibration point, the integrated signals of five calibration spots were averaged.

LA-ICP-SF MS analysis

All investigations were carried out using an NWR213 LA system equipped with a two-volume ablation chamber (ESI, Portland, USA) coupled to an inductively coupled plasma sector field mass spectrometer (ICP-SF-MS; Element XR, Thermo Fisher Scientific, Bremen, Germany). The ICP-SF-MS was synchronized using the LA unit in an external trigger mode. The slides with thin sections were mounted on the sample holder and inserted into a two-volume ablation chamber (New Wave 213). Two different laser scanning conditions were used here, which are described as follows.

Method 1 (for imaging): LA for imaging of the thin sections of the spheroids was achieved by conducting parallel line scans with a laser diameter of 8 μm, repetition rate of 20 Hz, and scanning speed of 8 μm s^{-1}. The distance between scan lines was 10 μm.

Method 2 (for calibration spots): A laser spot with a diameter of 175 μm and repetition rate of 20 Hz was used to completely ablate spots of the NP suspensions.

Table 1 Experimental parameters of the LA system (NWR213, ESI, Portland, USA) used for imaging of thin sections of MCSs, and single-spot ablation of calibration spots

Parameter	Imaging thin sections	Calibration spots
Carrier gas flow rate	1 L min^{-1} He	
Laser type	Nd:YAG	
Wavelength	213 nm	
Laser fluence	1.0 J cm^{-2}	
Repetition frequency	20 Hz	
Laser spot size	8 μm	175 μm
Laser warm up	5 s	
Ablation mode	Line scans (8 μm s^{-1}; 10-μm distance)	Single spot (ten single shots)

For all LA experiments, the same fluence of 1.0 J cm^{-2} was used. The aerosol was transported by helium at a flow rate of 1 L min^{-1} and argon was added in front of the ICP torch at a typical flow rate of 0.8 L min^{-1}. The LA-ICP-SFMS was tuned for maximum intensity of ^{137}Ba and ^{232}Th as well as low oxide ratio ((ThO/Th) < 3%) on a microscope glass slide by ablating line scans, which was carried out with the conditions: a laser diameter of 200 μm, maximum laser energy (6.0 J cm^{-2}) and scanning speed of 10 μm s^{-1}. All investigations were carried out on the same day within 9 h using the same tuning conditions of the ICP-SFMS. The applied mass spectrometer scanning conditions contained five isotopes (^{31}P, ^{63}Cu, ^{66}Zn, ^{79}Br, and ^{109}Ag), which were used for data acquisition with an integration time of 2 ms for each isotope. In this multi-isotope measurement mode, we are aware of data losses caused by the settling time of the magnet of the sector field device used here, which resulted in a total analysis time for one measurement cycle of 180 ms. Thus, for quantification only a single isotope, ^{109}Ag was measured in both the imaging and calibration modes to shorten the cycle time to 11 ms (integration time of 2 ms). The ICP-SFMS instrument was operated in a dual mode that

automatically switched to an analogue mode for intense signals. The exact ICP-MS operating conditions and data acquisition parameters for both methods are presented in detail in Table S1 (see Electronic Supplementary Material, ESM).

Morphological analysis

Staining with DAPI

DAPI solution was diluted with pure water to a concentration of 5 μg mL^{-1}. Thin sections of MCSs were treated with the diluted solution for 5 min and then washed twice with TBS. Fluorescence images were acquired using a fluorescence microscope (SZX16, Olympus, Tokyo, Japan) with a fluorescence filter cube (U-MWU2, Olympus).

Staining with aniline blue

Aniline blue solution was diluted with 1% acetic acid solution to give an aniline blue concentration of 0.1%. Thin sections of MCSs were treated with the diluted solution for 3 min and then washed three times with 1% acetic acid. Sample observation was carried out with an optical microscope (AE2000, Motic (Xiamen) Electric Group Co., Ltd., Xiamen, China).

Data analysis

The raw data of an LA-ICP-MS image consisted of a sequence of line scans. To visualize the raw data, the line scans for each element were transformed into a matrix (text image) using a customized Excel-macro program. This matrix was visualized using iQuant2, which was developed by Suzuki et al. [31] to obtain an image with the proper dimensions and a color-coded intensity scale. In most of the figures, a histogram of the measured color-coded intensities is shown. Additional information was provided in the software window of iQuant2, such as laser conditions, intensity minimum and maximum, dimension scaling, and linear or logarithmic representations of intensity. Extracted line profiles were carried out using ImageJ [32].

Results and discussion

Production of spheroids

Spheroid production was examined by changing the seeding cell number from 500 to 40,000 viable cells per well in a 96-well plate and then measuring the spheroid diameter after a growing period of 1 to 10 days. Figure 1 shows the diameter of MCSs with different seeding cell numbers (from 500 to 40,000 cells per well) after a growth period of 6 days. Each value represents the mean diameter of five spheroid samples (error bars are also shown) grown in the same 96-well plate.

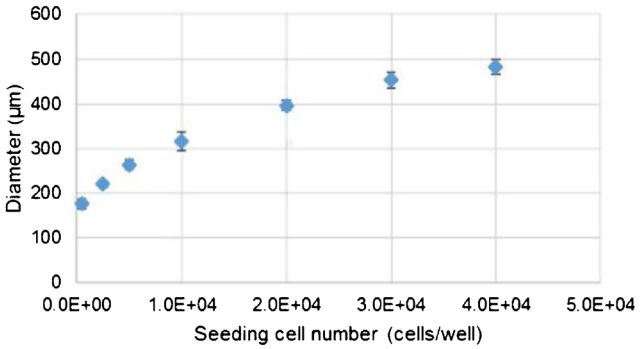

Fig. 1 MCS diameter after a growth period of 6 days as a function of seeding cell number. Error bars are the mean standard deviations of five samples

The low scatter of the diameter demonstrates that there was comparable parallel growth in all wells. The diameter increased linearly with seeding cell number at first and then started to saturate at about 500 μm for the highest seeding cell number investigated. The growth time dependence of the MCS diameter for samples with preselected seeding cell numbers is shown in Fig. S1 (see ESM). After a growth period of 6 days, the diameter of the spheroids became constant. The diameter of all spheroids decreased by more than 30% during the growth period from 0 to 6 days, whereas their changes from 6 to 10 days were less than ± 2%. Therefore, it was concluded that the cell diameter decreased until a final stable cell density was reached. We selected a growth period of 10 days in all further investigations to ensure that mature spheroid samples were used in all NP incubation experiments.

Qualitative measurement of thin sections

Thin sections with a thickness of 20 μm were produced from each MCS using a cryomicrotome. Although all different sections were measured, only the results from the center parts of MCSs are shown here. Photographs of the thin sections are shown in Fig. S2 (see ESM). For Fig. S2 c), the color based on the eosin stain was observed darker than others. It suggested that the MCS with lower seeding cell number and treated with Ag NPs for 24 h was affected by their exposure; however, further investigation is needed to answer this issue. On the other hand, the samples with higher seeding cell number, especially for the highest seeding cell number, look keeping their spherical shape. This was always observed in the samples, which were produced in parallel on the same day and on different days. Namely, it is suggested that MCSs with the higher seeding cell number used in this study are reproducible and are more robust against the influence of Ag NP exposure than one with lower seeding cell number. Thin sections except ESM Fig. S2 c) had a distinct ring-like outer shell with a thickness of around 20 μm (ESM Fig. S2f). The whole area of thin sections was then ablated by LA. Elemental images of the MCS with the highest seeding cell number are shown in

Fig. 2 as a representative example. ^{31}P, ^{63}Cu, and ^{66}Zn were measured to compare the localization of Ag NPs. The thin sections were completely ablated by the laser on the setup used in this study. All images except ^{109}Ag shown were subtracted with their background. Concerning the selection of elements of interest, we have to mention that we are limited in the number of isotopes selected for the measurements due to the low scanning speed of a sector field instrument. Thus, we have selected those isotopes that are of the highest biological relevance. P, Cu, and Zn are essential elements and are important to understand cell biological processes. In preliminary studies that are not reported here, we also tried to measure a few elements such as Fe; however, the signal to noise ratio was not high enough for meaningful results. Concerning ^{63}Cu, we have to mention that a spectral interference (such as $^{23}Na^{40}Ar$) cannot be separated in the low-resolution mode of our instrument from the signal of this isotope and the alternative isotope ^{65}Cu is buried in the background. ^{79}Br contained in the Eosin molecule ($C_{20}H_8Br_2N_2O_9$, molecular weight 647) was measured to simulate the behavior of small molecules. Here, we defined small molecules as compounds with a molecular weight below 1000 Da. As a result of ^{79}Br (Fig. 2d), although the incubation time was comparatively short (only for 1 min), Br signals were already diffused among the outer rim and even in the core of the fibroblast MCSs. This is not surprising because small molecules (e.g., nutrients) can rapidly diffuse and the diffusion limit of small molecules and nutrients is reported as about 200 μm [33]. Therefore, we can claim that Eosin can be used to simulate a behavior of small molecules among the fibroblast MCSs. Figure 2f shows an optical microscopy image of the spheroid thin section before the LA-ICP-MS analysis. The ^{31}P intensity is the highest at the outer rim of the spheroid. The ^{63}Cu signal is weak and only slightly higher than the background noise level for a laser spot size of 8 μm. Like ^{31}P, ^{66}Zn, and ^{79}Br are also enriched in the outer rim of the MSC, which has a ring shape in the 2D intensity distribution. Almost no ^{109}Ag signal was detected in the core of the MCS. The content of Ag was surprisingly high in the lower part of the rim zone (bottom of Fig. 2e), but because the spheroid was transferred into the cryomold by a pipette, any information about the orientation of the spheroid during NP incubation was lost. Also, in the repeated experiments, the same phenomenon has been observed for at least 5 separately produced MCSs. Such a local enrichment on one side of the spheroid could be generated by NP sedimentation. However, Drescher's group [34] showed that NP suspensions are stable in serum containing nutrients (DMEM + 10% FBS) and formation of aggregates and resulting sedimentation of NPs are suppressed by the negatively charged protein layers coating the NPs. However, Drescher's experiments were performed without a cell culture, so it is not clear if the presence of the MCS changes the equilibrium of the serum proteins in such a way that their stabilization effect is markedly weakened. Therefore, we can only report that we observed such an enriched zone, which might be caused by diffusion of NPs from the supernatant cell culture because NP diffusion to the side and bottom of the MCS was hindered by the wall of the container. To reasonably compare Ag NPs transport, the areas except the enriched zone would be investigated for further examination.

Figure 3 presents the line scan data for ^{31}P and ^{109}Ag along the red lines in Fig. S2a–e (see ESM). ^{31}P was used to visualize the location of cells in the MCS. For the untreated spheroid

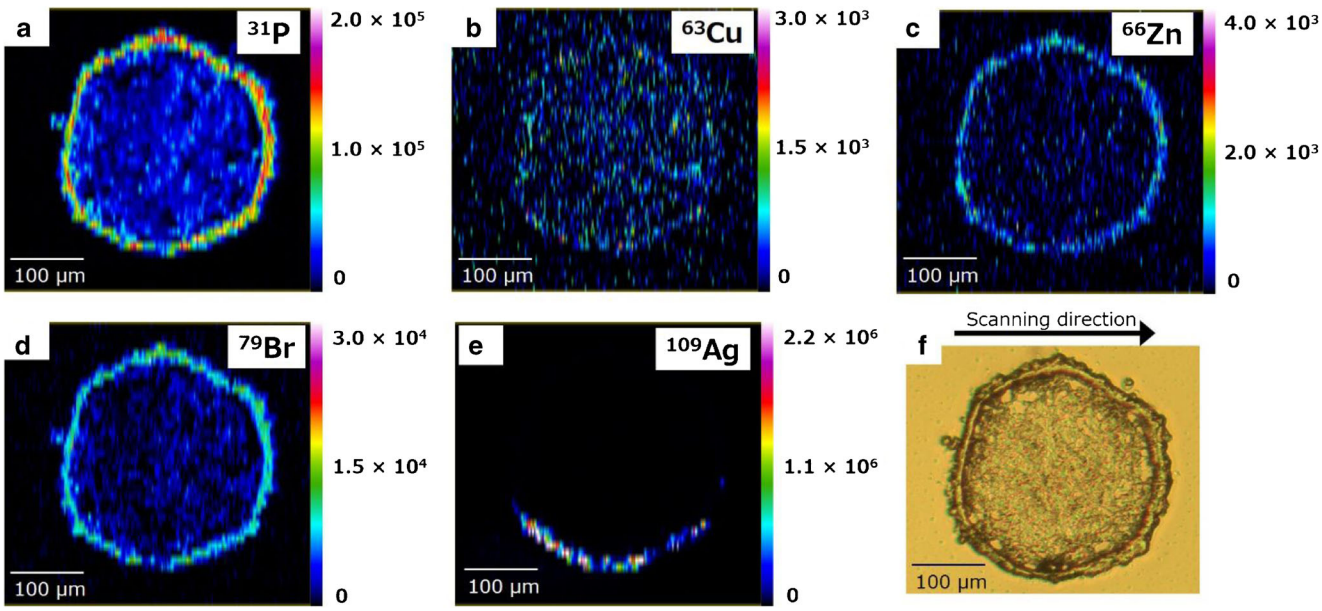

Fig. 2 Elemental and optical images of a thin section of an MCS sample (40,000 seeding cells per well with NP treatment for 24 h). Images show **a** ^{31}P, **b** ^{63}Cu, **c** ^{66}Zn, **d** ^{79}Br, and **e** ^{109}Ag with a color-coded scale based on signal counts of each isotope. Images except ^{109}Ag shown were subtracted with their background. **f** Bright-field microscopy image of the MCS section

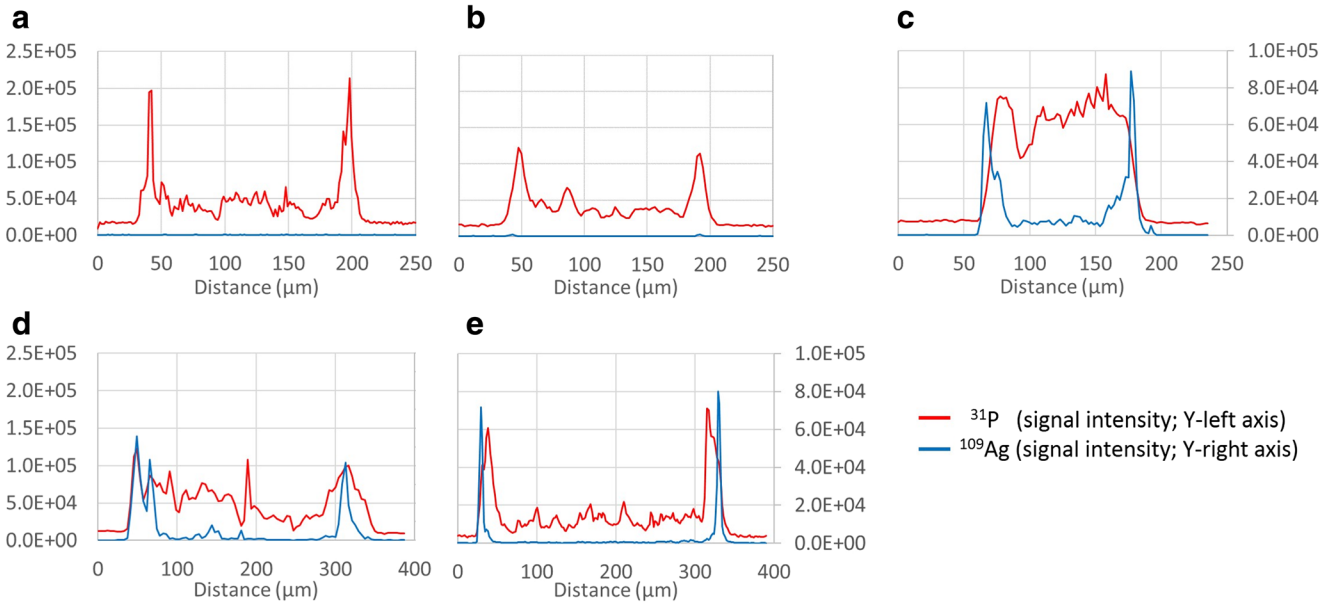

Fig. 3 Plots of signal intensities for ^{31}P and ^{109}Ag measured in line scans along the red lines shown in Fig. S2, ESM. **a** 10,000 cells per well without NP treatment, **b** 10,000 cells per well with NP treatment (incubation time of 3 h), **c** 10,000 cells per well with NP treatment (incubation time of 24 h), **d** 20,000 cells per well with NP treatment (incubation time of 24 h), and **e** 40,000 cells per well with NP treatment (incubation time of 24 h)

sample in Fig. 3a, only ^{31}P was detected above the background noise level; ^{109}Ag was not observed. In the center of the spheroid, P was distributed relatively homogenously, and it was enriched in the outer shell on both sides of the line scan. The highest ^{31}P intensity was nearly constant in Fig. 3a–e and the highest ^{31}P signal was always detected at the rim of the spheroid. After incubation of a spheroid for 3 h with Ag NPs (Fig. 3b), only a very weak signal consistent with ^{109}Ag was observed in the outer layer, which means that the adsorbed NPs were removed from the MCS surface by repeated washing with buffer solution. After increasing the incubation time to 24 h (Fig. 3c), clear signals of ^{109}Ag were observed, even in the core. However, the highest Ag intensity was still detected at the outer rim of the MCS. The Ag signal intensity was symmetric on both sides of the scan line, which is typical for a spherical structure. Increasing the seeding cell number to 20,000 cells per well while keeping the NP concentration and incubation time constant did not change the maximum peak intensity of ^{109}Ag at the outer rim but lowered the ^{109}Ag intensity in the MCS core (Fig. 3d). This effect of NP enrichment in the outer zone and depletion in the core became even more pronounced when the seeding cell number was raised to 40,000 cells per well (Fig. 3e). In this case, only a very sharp ^{109}Ag peak with a width of less than 10 µm was observed, whereas the width of this zone was in the range of 40 µm in Fig. 3c, d. Therefore, this zone is now even smaller than the enrichment zone visualized for ^{31}P, as shown in Fig. 3e. To allow comparison of these dimensions, we measured the diameter of the trypsinized fibroblast cells in a cell suspension before seeding into the 96-well plates (ESM Fig. S3). We obtained a value of 10.0 ± 1.7 µm, which is in good agreement with the diameter of the zone with a thickness of 9.6 µm in which Ag NPs are enriched (see ESM Fig. S6a). These findings indicate that Ag is concentrated in a thin layer with the dimension of a cell. However, we cannot claim that these particles are taken up by cells, because the outer layer has a rough surface which is equal to the thickness of one cell. Moreover, a small number of Ag NPs with a width of 9.7 µm was also observed that was consistent with co-localization in a second cell layer. However, this signal may also be a measurement artifact caused by the moonlike structure of overlapping circular laser spots in the line-scanning ablation mode, where the data acquisition was carried out every 180 ms (about 1.5 µm). Moreover, we have to consider that the mixing phenomenon during aerosol transport in the cell and in the tubing to the ICP-MS.

Calibration using spotted Ag NP suspensions

We used a NP suspension with a known number concentration to calibrate our measurements. The NP suspension was spotted onto a nitrocellulose membrane using an array spotter. The membrane was used for matrix matching due to the carbon rich substrate, which was already reported by Drescher et al. [20]. The calibration spots were ablated individually using a laser spot size of 175 µm, which was slightly larger than the diameter of each calibration spot (130 µm). This alternative procedure was used for calibration to improve the throughput of measurements. In principle, the signal intensity depends on the number of atoms of a NP introduced into the ICP and the mass detector, but not on the laser spot size. Therefore, in this study, a printing error for the lager laser diameter was used for calibration to improve not only throughput but statistics as well.

The more technical discussion is mentioned in the ESM. In summary, the slope of the calibration graph (ESM Fig. S4) is 2248 raw counts per NP, and the limit of detection calculated as 3σ is 0.7 Ag NP (φ 50 nm), so that the sensitivity is high enough to detect a single NP.

From the calibration, the Ag intensities shown in Fig. 3a–e can now be converted into the number of NPs in each pixel, which is shown in Fig. 4 with a full scale of particle number. A magnified view showing the range from one to five particles to illustrate how many particles are visible inside the spheroids is presented in Fig. S5 (see ESM). The short incubation time of 3 h gave a very small Ag signal (ESM Fig. S5b), which is ten times weaker than the intensity of a single NP and thus can be interpreted as ionic Ag. Bearing in mind that the total mass of Ag in a single Ag NP was only 0.68 fg, we then estimated that the amount of ionic Ag detected was at the low attogram level, which demonstrated the detection capability of LA-ICP-SFMS. Scanning along the red line in Fig. S2e (see ESM) after an incubation time of 24 h indicated that the number of NPs in the outer zone increased to about 30. This number of particles appeared to be independent of the seeding cell number. However, the width of the zone significantly decreased in the case of the highest seeding cell number. For seeding cell numbers of 10,000 and 20,000 cells per well, single Ag NP events were detected in the spheroid core (ESM Fig. S5c and d). For the highest seeding cell number of 40,000, no NP events were detected in the core; all NPs were trapped in the outer rim zone (ESM Fig. S6 a and c). Only some smaller signals at medium attogram levels were seen in the center (ESM Fig. S5e), which again is consistent with the presence of Ag^+. Fig. S6 (see ESM) reveals that the measured thickness of the outer zone is 20 μm. A magnified view showing the number of Ag NPs in this region is presented in Fig. S5e (see ESM). Most of the NPs are enriched in the outer rim layer with a thickness of less than 10 μm, which is close to a cell diameter. Only a small fraction of three NPs was detected in the second layer and no NPs were observed in the core under the conditions used (ESM Fig. S6a).

Concerning our calibration approach, the data presented in each pixel measured are quantitative; however, when using ICP-SFMS, we are limited by data losses caused by the predefined settling time of the magnet. For example, in the multi-isotope measurement mode shown in Fig. S7a and b (see ESM), the data cycle time for the five isotopes was about 180 ms including integration and settling times. This means that we could get a data point every three or four laser shots, which limited the local resolution. Additionally, the estimated data coverage for the Ag isotope is only ~ 1.1%. Of course, by increasing the integration time, one can improve the data coverage; however, we want to measure all isotopes from the same laser shot; thus, even shorter integration time is required. In this study, we chose 2 ms as the minimum integration time not to make the data coverage less than 1%. In the next experiment, we compared the results for a single isotope with those obtained in a multi-isotope measurement mode. In this experiment, only one isotope, as shown in Fig. S7c (see ESM), was measured. However, the magnet stabilization still took at least 9 ms, so a minimum cycle time of 11 ms was required. This approach markedly increased the data coverage to about 18% and allowed us to acquire four data points per single laser shot, so the local resolution was also improved. For this purpose, a thin section of an MCS grown in parallel to

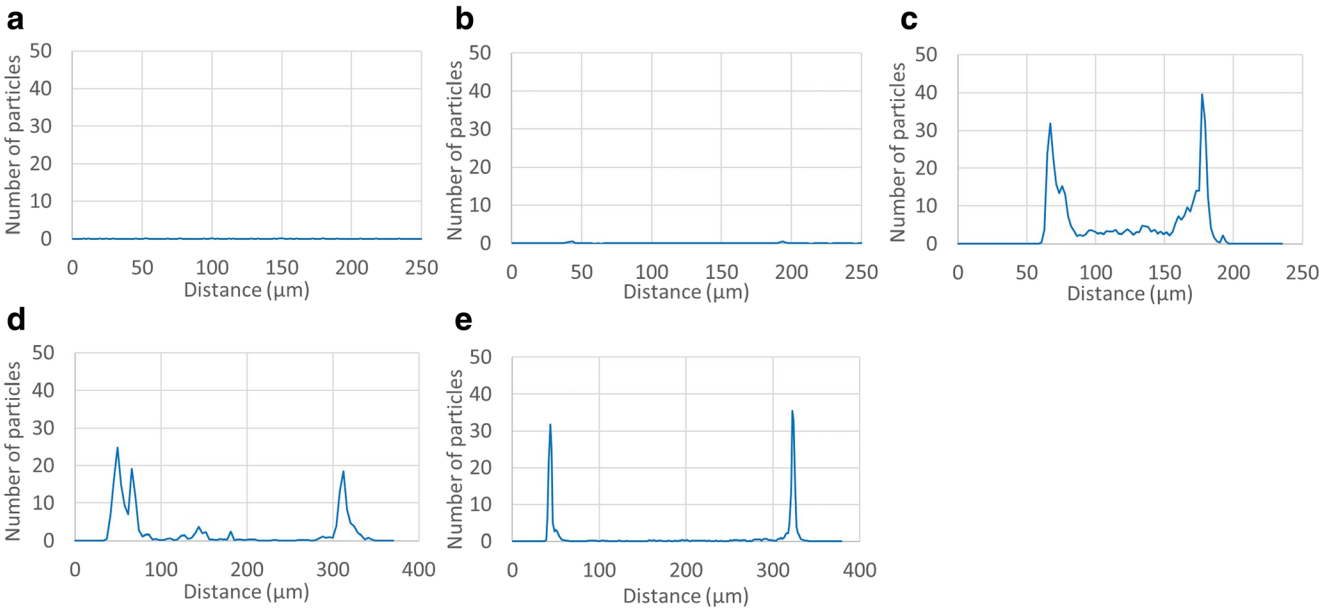

Fig. 4 Distribution of nanoparticles (NPs) along the line scan shown for Ag intensities in Fig. 3a–e using the calibration in Fig. S4, ESM. **a** 10,000 seeding cells per well without NP treatment, **b** 10,000 seeding cells per well with NP treatment for 3 h, **c** 10,000 seeding cells per well with NP treatment for 24 h, **d** 20,000 seeding cells per well with NP treatment for 24 h, and **e** 40,000 seeding cells per well with NP treatment for 24 h

those used in previous experiments was measured and quantified again using the method for a single-isotope measurement, which is identical to the measurement mode of a calibration spot. For comparison, the total integrated numbers of Ag NPs quantified by multi- and single-isotope modes are shown in Fig. S8 (see ESM). The data were extrapolated using 100% data coverage, which showed that the loss in the integrated NP number in two different thin sections of MCSs was less than 10%. In total, 0.4 million NPs were extrapolated for the tissue sample measured in the single-isotope mode. For validation, a tissue section of an MCS sample grown in parallel (optical photos are shown in ESM Fig. S9) was digested by acid digestion and then the total Ag content of 0.22 ng was determined. The total amount of a single Ag NP with a diameter of 50 nm is 0.68 fg. Multiplying this amount by the number of particles gave a total amount of 0.26 ng determined by LA-ICP-MS, which is in good agreement with the data obtained from the digested samples. Therefore, the calibration approach used for LA-ICP-MS allowed absolute calibration of Ag NPs in MCS tissue samples.

A lateral quantitative distribution of Ag NPs in the thin section from this parallel-grown MCS measured in the single-isotope mode is also shown in Fig. 5 as a birds-eye view, which is one of visualization tools in iQuant2 software. Again, as already shown in Fig. 2e, the NPs were localized in a ring-like structure and pronounced hot spots containing more than 7000 NPs in a single cell can be identified in the enriched zone. This value is in good agreement with the results for a 2D cell model (see ref. 19). Considering the results in Fig. 2, surprisingly, we see no significant effect to elemental distributions of P, Cu, and Zn in this enriched zone, which means that the biological reactions are not yet visible even though the particle numbers are so high.

Although we achieved a data coverage of about 20% with the sector field device in the latter experiment, the data presented in Fig. 5 are still not absolute values. Instead, they can be interpreted as minimum values, because the particle number could be much higher in a measurement with no data loss.

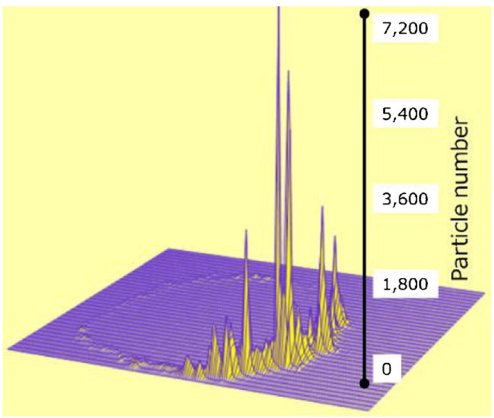

Fig. 5 Birds-eye view of Ag NP distribution with a scale bar showing the number of Ag NPs per data point

Such a measurement would be possible with a time-of-flight mass spectrometer, which would also give the additional advantage that all elements could be measured simultaneously. We hope to collect such absolute data in our future research.

Morphological study with DAPI and aniline blue staining

We observed very strong NP enrichment in a relatively thin layer with a thickness of two cell diameters, which is smaller than the P-rich zone of proliferating cells. To probe the composition of this layer, we used DAPI staining for a sample with the highest seeding cell number; the results are shown in ESM Fig. S10). The thin section depicted in Fig. S10 is that next to the one shown in the demonstration of the single-isotope mode. In the fluorescence image, the ring-like structure of the outer very active zone, which is rich in DNA and RNA, was visible as bright blue, and cells were also detected in the center of the core. Additionally, we performed aniline blue staining of another thin section of an MCS grown in parallel to those used in previous experiment, and the results are provided in Fig. S11 (see ESM). Here, the outer rim was again clearly visible as a bluer. In ESM Fig. S10b, single cells embedded in an extracellular matrix including collagens are visible. From this figure, the total thickness of the outer layer was estimated to be equivalent to about two cell diameters. For this spheroid, which had a seeding cell number of 40,000 cells per well, the transport of NPs suddenly changed and the penetration of the MCS was completely prevented by the presence of a cellular barrier. Only small molecules such as eosin with a molecular weight of 647 Da were detected in the spheroid core in this case. Therefore, this barrier with a thickness of two cell diameters (about 10 μm each) consisting of proliferating cells blocked NPs but did not suppress diffusion of small molecules.

We found that this barrier consisted of an extracellular matrix that was rich in collagen and some fibrous filaments, in which the fibroblast cells were embedded. A tight membrane was visible for the sample with the highest seeding cell number (see the results for aniline blue staining in ESM Fig. S11). Priwitaningrum et al. [27] also detected collagen-rich areas in MCSs, but they did not detect the formation of a membrane structure like that observed here. Namely, in that case, it suggests that the fibroblast MCSs used may be immature, which means fibroblast cell number is not enough to form this kind of membrane on MCSs.

At the outer rim of fibroblast MCSs matured, NPs behave quite differently to small molecules. Our previous work and that of some of our partners [34] revealed that NPs can be transported into fibroblast cells by endocytosis via membrane vesicles. However, the uptake of particles by this process has two prerequisites: first, particles must have a protein layer and second, they need to be in

direct contact with the membrane because uptake is regulated through surface receptors. Therefore, transport of endocytosis is a slow process in fibroblast cells and is not diffusion controlled. In our case, the particles cannot overcome the barrier of the MCS during the longest incubation time of 24 h studied here [35]. Thus, it might be of interest to extend the incubation time to determine the robustness of the barrier.

Conclusion

We have efficiently produced collagen-rich microstructures in fibroblast multicellular spheroids (MCSs) as a three-dimensional in vitro tissue analog to study transport of molecules and particles. Ag NPs and Eosin were used as probes to visualize the transport by elemental bioimaging by LA-ICP-MS. Overall, most particles were located in collagen-rich microstructures. Interestingly, in the case with the highest seeding cell number, the Ag NPs were localized in the outer rim zone only, whereas for samples with lower seeding cell numbers, penetration of NPs into the core was observed. This result indicates that a high enough seeding cell number is necessary to reproduce the collagen-rich microstructure in fibroblast MCSs as in vitro tissue analog resulting in a natural barrier for particle transport.

The quantitative results of the number of Ag NP up taken by a MCS measured in an imaging mode were in good agreement with the data from the acid digestion experiments.

The findings presented in this study will be of interest to simulate the transport of particulate materials (NPs or nanocarriers for drug delivery) in three-dimensional biological systems. The size-depending mechanism of trapping NPs in the biological barrier in contrast to small molecules will be investigated in more detail in our future work. For this purpose, we will decrease the NP size and increase the incubation period to test the robustness of the natural barrier. We also plan to increase the number of elements and avoid data losses by using a fast-scanning time-of-flight ICP-MS instrument. By this research, we hope to improve the resolution and absolute quantification capability of LA-ICP-MS to investigate interactions of nanoparticles to see if they affect the distribution of other elements in particular intrinsic minerals.

Acknowledgements We thank Konrad Löhr (Bundesanstalt für Materialforschung und -prüfung) for the support and training for the non-contact piezo-driven array spotter and Akvile Häckel (Charité Universitätsmedizin Berlin) for providing access to and support with using the cryomicrotome.

Compliance with ethical standards

Conflict of interest The authors declare that they have no conflicts of interest.

References

1. Kessler R. Engineered nanoparticles in consumer products: understanding a new ingredient. Environ Health Perspect. 2011;119(3):A120–A5.
2. Li W-R, Xie X-B, Shi Q-S, Zeng H-Y, OU-Yang Y-S, Chen Y-B. Antibacterial activity and mechanism of silver nanoparticles on Escherichia coli. Appl Microbiol Biotechnol. 2010;85(4):1115–22.
3. Larguinho M, Baptista PV. Gold and silver nanoparticles for clinical diagnostics - from genomics to proteomics. J Proteome. 2012;75(10):2811–23.
4. Wilkinson LJ, White RJ, Chipman JK. Silver and nanoparticles of silver in wound dressings: a review of efficacy and safety. J Wound Care. 2011;20(11):543–9.
5. Reidy B, Haase A, Luch A, Dawson K, Lynch I. Mechanisms of silver nanoparticle release, transformation and toxicity: a critical review of current knowledge and recommendations for future studies and applications. Materials. 2013;6(6):2295.
6. Aaron J, Travis K, Harrison N, Sokolov K. Dynamic imaging of molecular assemblies in live cells based on nanoparticle plasmon resonance coupling. Nano Lett. 2009;9(10):3612–8.
7. Ando J, Fujita K, Smith NI, Kawata S. Dynamic SERS imaging of cellular transport pathways with endocytosed gold nanoparticles. Nano Lett. 2011;11(12):5344–8.
8. Drescher D, Kneipp J. Nanomaterials in complex biological systems: insights from Raman spectroscopy. Chem Soc Rev. 2012;41(17):5780–99.
9. Kneipp J, Kneipp H, Rice WL, Kneipp K. Optical probes for biological applications based on surface-enhanced Raman scattering from indocyanine green on gold nanoparticles. Anal Chem. 2005;77(8):2381–5.
10. Huang X, Jain PK, El-Sayed IH, El-Sayed MA. Plasmonic photothermal therapy (PPTT) using gold nanoparticles. Lasers Med Sci. 2007;23(3):217.
11. Nam J, Won N, Jin H, Chung H, Kim S. pH-induced aggregation of gold nanoparticles for photothermal cancer therapy. J Am Chem Soc. 2009;131(38):13639–45.
12. Schneider G, Guttmann P, Heim S, Rehbein S, Mueller F, Nagashima K, et al. Three-dimensional cellular ultrastructure resolved by X-ray microscopy. Nat Methods. 2010;7:985.
13. Guehrs E, Schneider M, Günther CM, Hessing P, Heitz K, Wittke D, et al. Quantification of silver nanoparticle uptake and distribution within individual human macrophages by FIB/SEM slice and view. J Nanobiotechnol. 2017;15(1):21.
14. Alkilany AM, Murphy CJ. Toxicity and cellular uptake of gold nanoparticles: what we have learned so far? J Nanopart Res. 2010;12(7):2313–33.
15. Krystek P, Ulrich A, Garcia CC, Manohar S, Ritsema R. Application of plasma spectrometry for the analysis of engineered nanoparticles in suspensions and products. J Anal At Spectrom. 2011;26(9):1701–21.
16. Laux P, Tentschert J, Riebeling C, Braeuning A, Creutzenberg O, Epp A, et al. Nanomaterials: certain aspects of application, risk assessment and risk communication. Arch Toxicol. 2018;92(1):121–41.
17. Sabine Becker J, Matusch A, Palm C, Salber D, Morton KA, Susanne Becker J. Bioimaging of metals in brain tissue by laser ablation inductively coupled plasma mass spectrometry (LA-ICP-MS) and metallomics. Metallomics. 2010;2(2):104–11.
18. Van Acker T, Van Malderen SJM, Van Heerden M, McDuffie JE, Cuyckens F, Vanhaecke F. High-resolution laser ablation-inductively coupled plasma-mass spectrometry imaging of cisplatin-induced nephrotoxic side effects. Anal Chim Acta. 2016;945:23–30.

19. Giesen C, Waentig L, Mairinger T, Drescher D, Kneipp J, Roos PH, et al. Iodine as an elemental marker for imaging of single cells and tissue sections by laser ablation inductively coupled plasma mass spectrometry. J Anal At Spectrom. 2011;26(11):2160–5.
20. Drescher D, Giesen C, Traub H, Panne U, Kneipp J, Jakubowski N. Quantitative imaging of gold and silver nanoparticles in single eukaryotic cells by laser ablation ICP-MS. Anal Chem. 2012;84(22): 9684–8.
21. Scharlach C, Müller L, Wagner S, Kobayashi Y, Kratz H, Ebert M, et al. LA-ICP-MS allows quantitative microscopy of europium-doped iron oxide nanoparticles and is a possible alternative to ambiguous Prussian blue iron staining. J Biomed Nanotechnol. 2016;12(5):1001–10.
22. Büchner T, Drescher D, Traub H, Schrade P, Bachmann S, Jakubowski N, et al. Relating surface-enhanced Raman scattering signals of cells to gold nanoparticle aggregation as determined by LA-ICP-MS micromapping. Anal Bioanal Chem. 2014;406(27): 7003–14.
23. Drescher D, Zeise I, Traub H, Guttmann P, Seifert S, Büchner T, et al. In situ characterization of SiO2 nanoparticle biointeractions using BrightSilica. Adv Funct Mater. 2014;24(24):3765–75.
24. Theiner S, Schreiber-Brynzak E, Jakupec MA, Galanski M, Koellensperger G, Keppler BK. LA-ICP-MS imaging in multicellular tumor spheroids - a novel tool in the preclinical development of metal-based anticancer drugs. Metallomics. 2016;8(4):398–402.
25. Theiner S, Van Malderen SJM, Van Acker T, Legin A, Keppler BK, Vanhaecke F, et al. Fast high-resolution laser ablation-inductively coupled plasma mass spectrometry imaging of the distribution of platinum-based anticancer compounds in multicellular tumor spheroids. Anal Chem. 2017;89(23):12641–5.
26. Furukawa KS, Ushida T, Sakai Y, Kunii K, Suzuki M, Tanaka J, et al. Tissue-engineered skin using aggregates of normal human skin fibroblasts and biodegradable material. J Artif Organs. 2001;4(4):353–6.
27. Priwitaningrum DL, Blondé J-BG, Sridhar A, van Baarlen J, Hennink WE, Storm G, et al. Tumor stroma-containing 3D spheroid arrays: a tool to study nanoparticle penetration. J Control Release. 2016;244:257–68.
28. Jorgenson AJ, Choi KM, Sicard D, Smith KMJ, Hiemer SE, Varelas X, et al. TAZ activation drives fibroblast spheroid growth, expression of profibrotic paracrine signals, and context-dependent ECM gene expression. Am J Phys Cell Phys. 2017;312(3):C277–C85.
29. Sapudom J, Pompe T. Biomimetic tumor microenvironments based on collagen matrices. Biomater Sci. 2018;6(8):2009–24.
30. Emon B, Bauer J, Jain Y, Jung B, Saif T. Biophysics of tumor microenvironment and cancer metastasis - a mini review. Comput Struct Biotechnol J. 2018;16:279–87.
31. Suzuki T, Sakata S, Makino Y, Obayashi H, Ohara S, Hattori K, et al. iQuant2: software for rapid and quantitative imaging using laser ablation-ICP mass spectrometry. Mass Spectrom. 2018;7(1):A0065-A.
32. Schneider CA, Rasband WS, Eliceiri KW. NIH image to ImageJ: 25 years of image analysis. Nat Methods. 2012;9:671.
33. Curcio E, Salerno S, Barbieri G, De Bartolo L, Drioli E, Bader A. Mass transfer and metabolic reactions in hepatocyte spheroids cultured in rotating wall gas-permeable membrane system. Biomaterials. 2007;28(36):5487–97.
34. Drescher D. Spektro-Mikroskopische Charakterisierung von Nano-Bio-Wechselwirkungen in Zellen. PhD thesis. Humboldt University Berlin; 2016.
35. Drescher D, Guttmann P, Buchner T, Werner S, Laube G, Hornemann A, et al. Specific biomolecule corona is associated with ring-shaped organization of silver nanoparticles in cells. Nanoscale. 2013;5(19):9193–8.